

Dissipative Dynamics of Charged Graphene Quantum Batteries

Disha Verma,^{1,*} Indrajith VS,² and R. Sankaranarayanan¹

¹*Department of Physics, National Institute of Technology, Tiruchirappalli 620015, India.*

²*Qdit Labs Pvt. Ltd., Amruthahalli, Bangalore - 560092, India.*

We investigate dissipative dynamics in a graphene-based quantum battery modeled as a four-level spin-valley system. The battery is charged via a Gaussian pulse and subsequently evolves under amplitude damping, dephasing, and both Markovian and non-Markovian reservoirs. We find that amplitude damping, while inducing energy loss, can stabilize non-passive steady states with finite ergotropy, whereas pure dephasing suppresses coherence and eliminates work extraction. On the other hand, non-Markovian memory slows ergotropy loss and enables partial recovery through information backflow. These results identify coherence and reservoir memory as essential resources for enhancing the long-time performance of graphene quantum batteries.

I. INTRODUCTION

Rapid advancements in quantum information processing have fueled the search for novel nanomaterials that can operate within the quantum regime. Among these, graphene stands out as a promising platform due to its exceptional quantum properties, including high carrier mobility and long decoherence times, which make it ideal for quantum technologies. Understanding and exploiting quantum resources in graphene-based systems has therefore become a topic of growing interest.

Graphene is a two-dimensional material composed of carbon atoms arranged in a honeycomb lattice, first isolated by Geim and Novoselov in 2004 [1]. Its unique electronic properties arise from massless Dirac fermions originating from the two-sublattice structure of the lattice [2–5]. The low-energy states are concentrated near the inequivalent K and K' points in the Brillouin zone, introducing a valley degree of freedom. This valley pseudospin, combined with real spin, results in a rich internal state structure that supports exotic quantum phenomena such as the anomalous quantum Hall effect and minimal conductivity [1, 6]. The low-energy behavior of carriers in graphene is well described by a Dirac-like Hamiltonian derived from tight-binding approximations.

Quantum batteries (QBs) have emerged as a novel concept in quantum thermodynamics, capable of storing and delivering energy by harnessing quantum coherence and correlations. Theoretical studies have proposed a variety of QB models, including spin chains, cavity-QED systems, and many-body setups [7–11], while recent experiments have demonstrated proof-of-concept implementations [12–14]. Similar to classical batteries, a QB operates through three main stages: charging, storage, and discharging. Charging is typically achieved via a time-dependent interaction Hamiltonian, \mathcal{H}_1 , applied over a finite duration τ_c , during which the system \mathcal{H}_0 evolves according to the time-dependent Schrödinger equation. When $[\mathcal{H}_0, \mathcal{H}_1] \neq 0$, the charging dynamics are non-trivial, enabling energy transfer into the system.

In realistic scenarios, QBs are open quantum systems due to unavoidable interactions with their environments. To address this, various studies have explored robust states and protocols for mitigating decoherence and retaining extractable work (ergotropy) [15, 16]. A detailed review of open-system QBs can be found in [17].

To ensure the physical relevance of our model, we emphasize that the spin-valley tensor states in graphene are not mere theoretical constructs but have been realized and controlled experimentally. Graphene nanostructures, including quantum dots and SNS (superconductor-normal metal-superconductor) junctions, have demonstrated tunable spin and valley degrees of freedom [18, 19]. Moreover, proximity-induced superconductivity in graphene SNS junctions enables phase-sensitive manipulation of Andreev bound states carrying spin and valley indices [20]. Valleytronics studies have further shown that the K/K' valleys can serve as computational bases, with selective excitation achieved using circularly polarized light [21]. These developments provide a strong experimental foundation for graphene-based quantum battery designs.

Motivated by these advances, we propose a four-level graphene quantum battery model based on spin-valley coupled qubits, where charging is induced via a Gaussian pulse in a closed system. Following the charging phase, we investigate the effects of environmental dissipation modeled by both Markovian and non-Markovian amplitude damping channels. This approach allows us to evaluate the intrinsic performance of the battery, as well as the retention of ergotropy under realistic open-system conditions. Similar pulse-based charging protocols and dissipation analyses have been studied in the context of quantum thermodynamics [22–24], providing a firm theoretical foundation for our work.

II. MODEL

A. Graphene-Based Quantum Battery

In monolayer graphene, the low-energy electronic structure arises from two inequivalent sublattices (A and

* vermadisha785@gmail.com

B) and two valleys (K and K') in the Brillouin zone. These internal degrees of freedom can be described using two sets of Pauli matrices: $\vec{\sigma} = (\sigma_x, \sigma_y, \sigma_z)$ acting on the sublattice pseudospin, and $\vec{\tau} = (\tau_x, \tau_y, \tau_z)$ acting on the valley pseudospin. The combined Hilbert space is four-dimensional, spanned by the basis $\{|00\rangle, |01\rangle, |10\rangle, |11\rangle\}$, where the first (second) index labels the sublattice (valley) degree of freedom. Within the effective-mass approximation near the Dirac points, the low-energy Hamiltonian is written as [25]

$$H_0 = \eta[n_x(\sigma_x \otimes I_2) + n_y(\sigma_y \otimes \tau_z)] + H_{\text{int}}, \quad (1)$$

where η sets the kinetic energy scale related to the Fermi velocity, and n_x, n_y introduce momentum-dependent asymmetry between the off-diagonal couplings. H_{int} incorporates inter-sublattice and inter-valley couplings.

The interaction between the sublattice and valley pseudospins in graphene can be expressed as

$$H_{\text{int}} = \lambda(I_4 + e^{-i\alpha}\sigma_+ \otimes I_2 + e^{i\alpha}\sigma_- \otimes I_2), \quad (2)$$

where λ sets the characteristic interaction strength and α represents an anisotropy phase between inter-sublattice couplings. Here, $\sigma_{\pm} = (\sigma_x \pm i\sigma_y)/2$ act on the sublattice pseudospin space, while I_2 is the identity in the valley subspace. The first term, proportional to I_4 , corresponds to on-site intravalley contributions, whereas the remaining terms describe inter-sublattice tunneling processes with a complex phase factor $e^{\pm i\alpha}$. This phase controls the direction-dependent hybridization between sublattice states, introducing an effective anisotropy in the coupling. Combining Eqs. (1)–(2) gives the effective four-level Hamiltonian matrix

$$H_0 = \lambda \begin{pmatrix} 1 & e^{-i\alpha} & \tilde{\eta}(n_x - in_y) & 0 \\ e^{i\alpha} & 1 & 0 & \tilde{\eta}(n_x + in_y) \\ \tilde{\eta}(n_x + in_y) & 0 & 1 & e^{-i\alpha} \\ 0 & \tilde{\eta}(n_x - in_y) & e^{i\alpha} & 1 \end{pmatrix}, \quad (3)$$

where $\tilde{\eta} = \eta/\lambda$ quantifies the relative coupling strength.

Diagonalization of Eq. (3) yields four eigenstates :

$$|\phi_1\rangle = e^{-i\alpha}A_+|00\rangle + \frac{1}{2}|01\rangle + \frac{1}{2}e^{-i\alpha}|10\rangle + A_+|11\rangle, \quad (4)$$

$$|\phi_2\rangle = -e^{-i\alpha}A_+|00\rangle + \frac{1}{2}|01\rangle + \frac{1}{2}e^{-i\alpha}|10\rangle - A_+|11\rangle, \quad (5)$$

$$|\phi_3\rangle = -\frac{1}{2}e^{-i\alpha}|00\rangle + A_-|01\rangle - e^{-i\alpha}A_-|10\rangle + \frac{1}{2}|11\rangle, \quad (6)$$

$$|\phi_4\rangle = -\frac{1}{2}e^{-i\alpha}|00\rangle - A_-|01\rangle + e^{-i\alpha}A_-|10\rangle + \frac{1}{2}|11\rangle, \quad (7)$$

where

$$A_{\pm} = -\frac{k_1 \pm 1 \mp ik_2}{2\sqrt{1 + k_1^2 \pm 2k_1 + k_2^2}}, \quad k_1 = \frac{\eta n_x}{\lambda}, \quad k_2 = \frac{\eta n_y}{\lambda}. \quad (8)$$

The corresponding energy eigenvalues are

$$E_1 = \lambda \left(1 - \sqrt{1 + k_1^2 + 2k_1 + k_2^2} \right), \quad (9)$$

$$E_2 = \lambda \left(1 + \sqrt{1 + k_1^2 + 2k_1 + k_2^2} \right), \quad (10)$$

$$E_3 = \lambda \left(1 - \sqrt{1 + k_1^2 - 2k_1 + k_2^2} \right), \quad (11)$$

$$E_4 = \lambda \left(1 + \sqrt{1 + k_1^2 - 2k_1 + k_2^2} \right). \quad (12)$$

These four eigenvalues define the discrete energy spectrum of the graphene-based quantum battery. Throughout this analysis, η , λ , n_x , and n_y are treated as dimensionless quantities for convenience.

B. Charging Protocol

The battery is initialized in the ground state of the system Hamiltonian H_0 , obtained by solving:

$$H_0|\psi_{GS}\rangle = E_{GS}|\psi_{GS}\rangle, \quad (13)$$

with the corresponding density matrix given by $\rho_0 = |\psi_{GS}\rangle\langle\psi_{GS}|$.

The charging process is driven by an external, time-dependent Gaussian pulse field represented as

$$H_{\text{pulse}}(t) = B_s \begin{pmatrix} 1 & 0 & 0 & 0 \\ 0 & -1 & 0 & 0 \\ 0 & 0 & 1 & 0 \\ 0 & 0 & 0 & -1 \end{pmatrix} e^{-t^2/(2\tau^2)}, \quad (14)$$

The chosen pulse Hamiltonian is analogous to a longitudinal Zeeman interaction, where the diagonal form induces opposite energy shifts for states of opposite spin or pseudospin orientation. Such a coupling alters the energy spectrum without causing inter-state transitions, thereby preserving phase coherence during the charging dynamics. This results in a coherent, reversible energy injection process that can be experimentally realized through spin- or valley-selective electrostatic or magnetic field in graphene-based systems. Here, t denotes time, governing the temporal evolution of the charging process, while τ characterizes the pulse width and thus the duration of the external drive. A smaller τ corresponds to a faster, more localized pulse. In this study, $\tau = 1.0$ is chosen as a normalized time scale to represent a fast charging process within a short interaction window. A larger B_s produces stronger driving and faster population transfer between energy levels.

Gaussian pulses are commonly used in quantum control and thermodynamic processes because they are experimentally feasible and minimize abrupt transitions that could cause unwanted excitations [12, 26, 27]. The total time-dependent Hamiltonian governing the charging process is thus

$$H(t) = H_0 + H_{\text{pulse}}(t), \quad (15)$$

. The applied pulse coherently drives transitions between eigenstates of H_0 , effectively transferring energy into the system and charging the quantum battery.

III. OBSERVABLES

To analyze the charging and dissipation dynamics of the graphene quantum battery, we evaluate key physical quantities that characterize its energetic and quantum properties. These include the stored energy, fidelity-based purity, and the ergotropy, which together provide a comprehensive picture of the battery's performance under different environmental interactions.

A. Energy and Purity

The instantaneous energy of the system is given by

$$\langle H_0 \rangle = \text{Tr}[H_0 \rho(t)], \quad (16)$$

where H_0 denotes the system Hamiltonian and $\rho(t)$ is the time-evolved density matrix. This expectation value represents the total stored energy within the battery at time t .

To quantify the purity, we employ the fidelity-based purity measure [28], defined as

$$P_F(\rho) = \log_d(d \text{Tr}[\rho(t)^2]), \quad (17)$$

where d is the Hilbert-space dimension of the system. This purity measure indeed has intricate connection to the quantum coherence. This logarithmic normalization renders $P_F(\rho)$ dimension-independent and bounded, providing an intuitive interpretation of mixedness: $P_F(\rho) = 1$ for a perfectly coherent pure state and $P_F(\rho) < 1$ as mixedness sets in. Together, the quantities $\langle H_0 \rangle$ and $P_F(\rho)$ capture the interplay between energetic retention and coherence degradation that governs the operational efficiency of the battery.

B. Ergotropy

The extractable work content of a quantum state is quantified by its *ergotropy*, which represents the maximum amount of work obtainable through unitary operations without changing the state's entropy. For a time-dependent Hamiltonian $H(t)$ and a corresponding density matrix $\rho(t)$, the ergotropy is defined as

$$\mathcal{E}(t) = \text{Tr}[H(t)\rho(t)] - \text{Tr}[H(t)\rho_{\text{passive}}(t)], \quad (18)$$

where $\rho_{\text{passive}}(t)$ is the passive counterpart of $\rho(t)$ with respect to $H(t)$. The passive state $\rho_{\text{passive}}(t)$ is constructed by arranging the eigenvalues of the density matrix $\rho(t)$ in decreasing order and assigning them to the eigenstates

of $H(t)$ in increasing order of energy:

$$\rho_{\text{passive}}(t) = \sum_i p_i^\downarrow |E_i^\uparrow\rangle \langle E_i^\uparrow|, \quad (19)$$

where p_i^\downarrow are the eigenvalues of $\rho(t)$ sorted in descending order, and $|E_i^\uparrow\rangle$ are the eigenstates of $H(t)$ arranged in ascending order of energy [29, 30]. The passive state shares the same spectrum as $\rho(t)$ but has zero extractable work.

For a closed system, the evolution is purely unitary,

$$\rho(t) = U(t)\rho_0 U^\dagger(t), \quad (20)$$

with

$$U(t) = \mathcal{T} \exp \left[-i \int_0^t H(s) ds \right], \quad (21)$$

where \mathcal{T} denotes time ordering. Since entropy remains constant under unitary evolution, any energy gain directly contributes to ergotropy.

In open-system scenarios, interactions with an external environment induce non-unitary evolution governed by the Lindblad master equation,

$$\dot{\rho}(t) = -i[H(t), \rho(t)] + \gamma \mathcal{D}[L]\rho(t), \quad (22)$$

where $\mathcal{D}[L]\rho = L\rho L^\dagger - \frac{1}{2}\{L^\dagger L, \rho\}$ denotes the dissipator associated with the channel L , γ represents the dissipation strength and $\{A, B\} = AB + BA$ represents the anticommutator between operators A and B . The evolution of the system's density matrix $\rho(t)$ is governed by the Lindblad master equation [31–33]. The instantaneous mixed state $\rho(t)$ obtained by numerically solving eq.(22) is then used to compute the ergotropy $\mathcal{E}(t)$ at each time step.

Thus, by jointly analyzing $\langle H_0 \rangle$, $P_F(\rho)$, and $\mathcal{E}(t)$, we obtain a complete dynamical characterization of the battery's energy retention, coherence evolution, and useful work capacity under realistic dissipative conditions.

IV. RESULTS

The parameters of the Hamiltonian in eq.(1) are chosen to ensure a balanced and physically realistic energy landscape for the four-level graphene quantum battery. The coupling constant λ sets the overall energy scale, while the phase parameter α introduces a complex phase factor ($e^{\pm i\alpha}$) in the interaction terms of eq.(3). This phase breaks the perfect symmetry between the two graphene sublattices, inducing controlled anisotropy in the coupling strengths. Setting $\alpha = \pi/4$ yields a moderate imbalance that preserves coherence while generating nontrivial interference between transition pathways—an essential feature for sustaining quantum coherence and nonzero ergotropy during the charging process.

The ratio $\eta = 0.5$ defines the relative strength between the kinetic and interaction contributions, ensuring a stable and well-separated eigenvalue spectrum. The asymmetric choice of momentum components, $n_x = 1$ and $n_y = 5$, represents anisotropic quasiparticle propagation within the graphene plane. This asymmetry breaks degeneracy among the energy levels, enriching the dynamical response of the system and enhancing the diversity of accessible transition channels. Collectively, these parameter choices capture realistic graphene band anisotropy and coherent coupling while maintaining numerical stability and analytical tractability.

Charging of the graphene quantum battery is achieved through a time-dependent Gaussian pulse field described by the Hamiltonian in eq.(14). The system is initially prepared in the ground state of H_0 and subsequently evolves under the total Hamiltonian $H(t)$ during the charging phase. As the process is closed and unitary, the evolution follows eq.(20), ensuring reversible and coherent energy storage.

A. Effect of Dissipation Strength

After charging, the quantum battery interacts with its environment, leading to decoherence. In our model, the environment is described by a Markovian amplitude damping (AD) channel characterized by spontaneous emission without thermal excitation. This corresponds to a zero-temperature reservoir, where population can decay from the excited to ground state but not vice versa. The corresponding collapse operator for the two-qubit system is defined as:

$$L_{AD} = (\sigma_- \otimes I + I \otimes \sigma_-), \quad (23)$$

where σ_- is the lowering (annihilation) operator for a single qubit.

The influence of dissipation strength on the graphene quantum battery reveals a subtle interplay between energy retention, coherence decay, and ergotropy stabilization. To quantify coherence, we employ the ℓ_1 -norm measure [34], defined as

$$C_{\ell_1}(\rho) = \sum_{i \neq j} |\rho_{ij}|, \quad (24)$$

which captures the contribution of all off-diagonal terms of the density matrix. (Refer to appendix A,B and C)

The overall analysis of Fig.1 shows that For **weak dissipation** ($\gamma = 0.1$), the stored energy builds up during charging as the dissipation strength is weak, leading to a high energy storage with time. Purity decreases gradually, reflecting persistent but slow decoherence. Inspection of the density matrices shows that the off-diagonal components (responsible for quantum coherence) diminish strongly, with ℓ_1 -coherence dropping from $C_{\ell_1} \approx 2.10$ at $t = 0$ to $C_{\ell_1} \approx 1.37$ at $t = 10$, and further down

to $C_{\ell_1} \approx 0.47$ by $t = 100$. Meanwhile, diagonal populations redistribute toward near-equilibrium values, rendering the state close to passive. Consequently, the ergotropy decays from $\mathcal{E}(t) \approx 1.81$ at $t = 0$ to $\mathcal{E}(t) \approx 0.92$ at $t = 10$, and finally vanishes asymptotically ($\mathcal{E}(t) \approx 0.17$ at $t = 100$), even though residual stored energy remains.

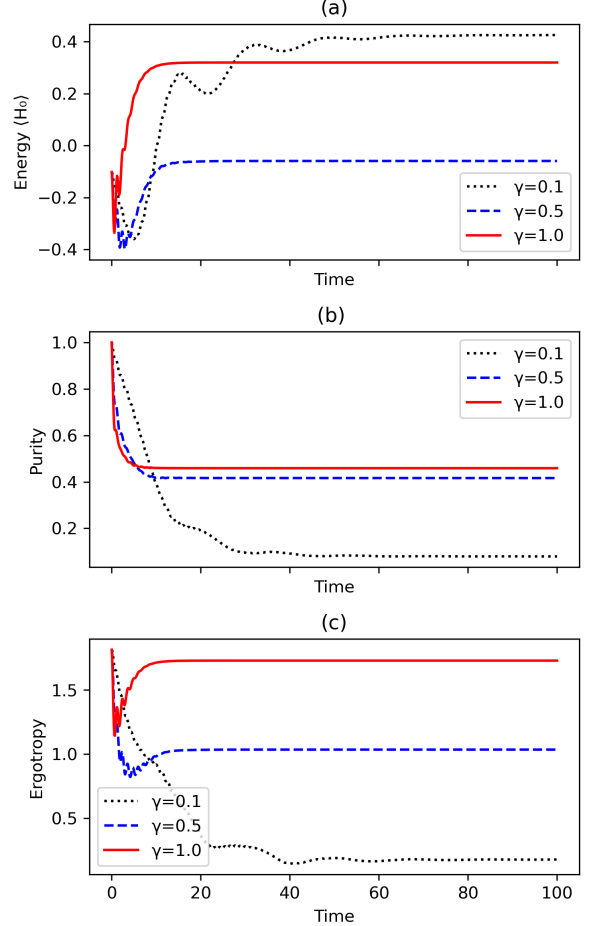


FIG. 1: Time evolution of (a) energy, (b) purity, and (c) ergotropy for different dissipation strengths $\gamma = 0.1$, 0.5 , and 1.0 .

For **intermediate dissipation** ($\gamma = 0.5$), the system loses energy more rapidly than in the weak case, but equilibration occurs at a finite steady value rather than full decay. Purity degrades faster, indicating stronger system–environment entanglement. Coherence is reduced by nearly half, from $C_{\ell_1} \approx 2.10$ at $t = 0$ to $C_{\ell_1} \approx 1.00$ by $t = 40$ – 100 , while diagonal populations remain noticeably imbalanced. This incomplete thermalization preserves a moderate ergotropy plateau: $\mathcal{E}(t)$ drops sharply to ≈ 0.98 at $t = 10$, but then stabilizes at $\mathcal{E}(t) \approx 1.03$ for long times ($t \geq 40$). Thus, intermediate damping achieves a balance: destructive coherences are suppressed, while population asymmetries survive long enough to sustain useful work extraction.

In the case of **strong dissipation** ($\gamma = 1.0$), the

stored energy relaxes quickly but saturates at a higher steady value than in the $\gamma = 0.5$ case. This counterintuitive effect arises from dissipation-assisted stabilization: fast damping suppresses harmful oscillations and selectively freezes favorable population distributions. Purity drops sharply at short times and then stabilizes. Although coherence collapses rapidly ($C_{\ell_1} \approx 2.10$ at $t = 0$, to $C_{\ell_1} \approx 0.89$ already by $t = 10$, and then remains nearly constant thereafter), the diagonal populations stabilize in a robustly non-passive arrangement, where ρ_{00} and ρ_{22} dominate over ρ_{11} and ρ_{33} . This locked imbalance maintains a significant fraction of extractable work, explaining why ergotropy stabilizes at the **highest asymptotic value**, $\mathcal{E}(t) \approx 1.73$ (observed from $t = 40$ onward).

Overall, these results demonstrate that dissipation does not universally degrade performance. Weak dissipation prolongs coherence but ultimately drives the system to passivity and negligible ergotropy. Intermediate dissipation balances coherence suppression with partial population retention, yielding moderate work. Strong dissipation, paradoxically, enhances long-time ergotropy by eliminating harmful coherences while preserving favorable population imbalances. This dissipation-assisted stabilization mechanism, also observed in related studies [30, 35, 36], highlights the possibility of harnessing structured environments to optimize ergotropy retention and work capacity in graphene-based quantum batteries.

B. Amplitude Damping and Dephasing

In the dissipative phase following coherent charging, two types of environmental noise are considered: amplitude damping (AD) and pure dephasing (Deph). These noise channels are modeled using Lindblad-type master equations with distinct collapse operators that characterize their physical effects. For amplitude damping, the system loses both energy and coherence due to irreversible excitation decay. The corresponding collapse operator is given by eq.(23), where $\sigma_- \otimes I$ denotes amplitude damping on the first qubit while $I \otimes \sigma_-$ applies it to the second. Their sum models collective amplitude damping on both qubits. This operator captures the decay processes that remove excitations from the system [31, 37]. In contrast, dephasing is modeled using the collapse operator

$$L_{\text{Deph}} = (\sigma_z \otimes I + I \otimes \sigma_z) \quad (25)$$

which affects only the coherence (off-diagonal elements of the density matrix) while preserving the populations. Since the operator is diagonal in the computational basis $|00\rangle, |01\rangle, |10\rangle, |11\rangle$, it results in pure phase decoherence without energy loss [33, 38].

Fig.2 presents a comparative analysis of the time evolution of ergotropy for a graphene-based quantum battery subject to amplitude damping (AD) and pure dephasing (Deph) at representative dissipation strengths $\gamma = 0.1, 0.5$, and 1.0 . In the AD case Fig.2(a), all γ values exhibit

an initial ergotropy build-up due to coherent charging, followed by decay as dissipation acts. For weak damping ($\gamma = 0.1$), excitations leak slowly into the reservoir and coherence decays gradually, driving the state toward passivity with negligible long-time ergotropy ($\mathcal{E}(t) \approx 0.18$). At intermediate damping ($\gamma = 0.5$), destructive coherences are suppressed while population imbalance persists, resulting in a finite ergotropy plateau. Remarkably, strong damping ($\gamma = 1.0$) yields the *highest* steady-state ergotropy, as rapid dissipation freezes favorable population distributions despite substantial coherence loss.

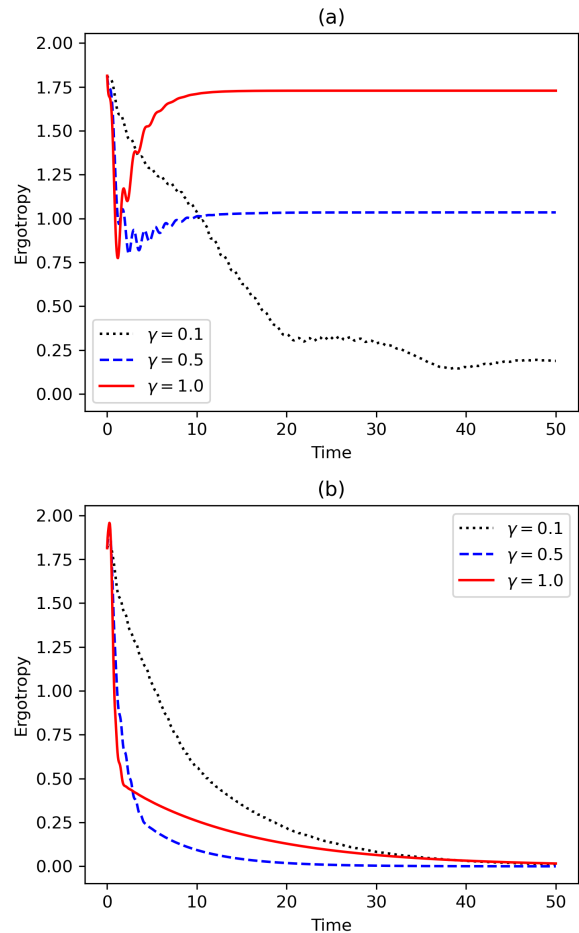


FIG. 2: Comparison of ergotropy evolution for different dissipation rates γ under (a) amplitude damping and (b) dephasing noise models.

In contrast, Deph Fig. 2(b) consistently destroys quantum advantage: coherence collapses rapidly ($C_{\ell_1} \rightarrow 0$) and the system diagonalizes in the energy eigenbasis, evolving into a maximally mixed, fully passive state with vanishing ergotropy, irrespective of γ . This leads to a strong decay in ergotropy to go from $\mathcal{E}(t) \approx 1.81$ at $t = 0$ to $\mathcal{E}(t) \approx 0.0001$ at $t = 100$ for a weak dissipation ($\gamma = 0.1$) and $\mathcal{E}(t) \approx 0.0008$ at $t = 100$ for a strong dissipation ($\gamma = 1.0$).

These contrasting behaviors underscore the thermo-

dynamic distinction between coherence-destroying and energy-relaxing channels. While amplitude damping involves energy leakage, it can paradoxically *enhances* ergotropy retention by stabilizing structured, non-passive steady states. Dephasing, despite conserving energy, irreversibly eliminates coherence and forces equilibration into passive configurations with negligible extractable work. Thus, ergotropy preservation is governed not solely by weak system–environment coupling but crucially by the *nature of dissipation*: AD can be harnessed as a resource for long-time work storage, whereas Deph invariably suppresses it [29, 39, 40].

C. Markovian vs Non-Markovian Dissipation

To understand how environmental memory influences the performance of the graphene quantum battery, we compare the dynamics generated by a standard Markovian Lindblad master equation with those arising from a time-dependent, non-Markovian dissipation model. The Markovian evolution corresponds to a constant decay rate γ and describes a memoryless reservoir that irreversibly drains excitations and coherence. In contrast, the non-Markovian scenario incorporates temporal correlations through a decay rate of the form

$$\gamma(t) = \gamma_0 e^{-\beta t} \cos(\omega t), \quad (26)$$

which enables information and energy to intermittently flow back into the system. The parameters γ_0 , β , and ω respectively control the initial coupling strength, the decay of memory, and the oscillatory character of the reservoir correlations. Each value of β therefore corresponds to a distinct memory timescale, with smaller β indicating strong and long-lasting environmental memory.

Energy Dynamics. Figure 3(a) shows the evolution of stored energy under Markovian and non-Markovian dissipation. In the Markovian case (black dashed), the energy exhibits a sharp dip to nearly -0.38 at short times, followed by a gradual recovery and stabilization slightly below zero. This behavior reflects rapid initial excitation loss into a memoryless bath and subsequent equilibration governed by a constant decay rate.

The non-Markovian curves reveal distinct trends depending on the memory parameter β . For strong memory ($\beta = 0.1$ (dotted)), the environment remains effectively coupled to the system for longer durations, leading to substantial early-time backflow. As a result, the energy rises sharply and eventually stabilizes at a positive value near 0.40 , indicating that the bath temporarily returns excitations to the battery. For moderate memory strengths ($\beta = 0.5$ (dot-dashed) and 1.0 (solid)), the time-dependent decay rate is more rapid, suppressing the backflow effect yet still producing non-Markovian modulation of the dynamics. In these cases, the energy settles at lower values (approximately -0.28 to -0.30), remaining below the Markovian steady state but exhibiting smoother relaxation and reduced early-time fluctua-

tions. These behaviors highlight that the energy response is highly sensitive to the duration of the system–bath coupling, with strong memory enabling pronounced energy inflow and moderate memory yielding more stabilized—but less enhanced—energy profiles.

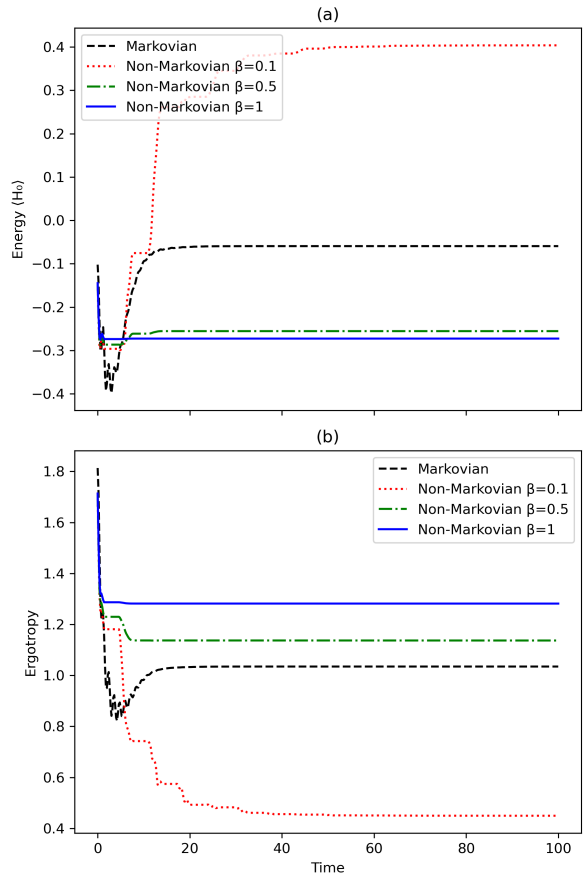


FIG. 3: Comparison of energy and ergotropy evolution for markovian and non markovian (solid for $\beta = 0.1, 0.5, 1.0$) environment ($\gamma_0 = 0.5, \omega = 1$).

Ergotropy Dynamics. Figure 3(b) shows the ergotropy under Markovian and non-Markovian dissipation. In the Markovian case (black dashed), ergotropy rapidly decreases to values around 0.8 before gradually recovering and stabilizing near 1.05, reflecting irreversible coherence loss in a memoryless environment. The non-Markovian profiles exhibit a different behavior. For strong memory ($\beta = 0.1$), the system remains strongly coupled to the environment for an extended duration, and the initial backflow is insufficient to preserve useful work; consequently, the ergotropy steadily decays and saturates near 0.4. For moderate memory strengths ($\beta = 0.5$ and 1.0), however, the time-dependent decay rate retains significant value while still allowing for coherence revival. In these regimes, information backflow counteracts dissipation, enabling the ergotropy to stabilize at values (1.15–1.30) substantially higher than those achieved under Markovian evolution. These cases repre-

sent non-Markovian enhancement, as the environment's finite memory actively contributes to preserving coherence and supporting extractable work. We note that very large values of the memory parameter suppress the decay rate so rapidly that the system effectively allows the coherence generated during charging to remain largely preserved resulting in increased ergotropy (Appendix C).

In summary, the plotted results reveal an interplay between environmental memory and battery performance. While extremely strong memory ($\beta = 0.1$) can induce energy inflow but degrade long-term ergotropy, moderate-to-weak memory ($\beta = 0.5, 1.0$) enables the system to maintain substantially higher extractable work than in the Markovian case. These findings highlight the potential of engineered non-Markovian reservoirs to selectively enhance ergotropy preservation and optimize long-time quantum battery operation.

V. CONCLUSION

In this work, we have analyzed the dissipative dynamics of a pulse-driven graphene-based quantum battery modeled as a four-level spin-valley coupled system. Charging was implemented via a Gaussian pulse, which enabled coherent population transfer and efficient energy storage under closed-system dynamics. The study of open-system effects revealed the intricate interplay between energy dissipation, coherence degradation, and ergotropy retention.

Our analysis of different noise channels shows that amplitude damping (AD) and dephasing (DP) have qualitatively distinct impacts. While AD causes both energy leakage and coherence decay, it can stabilize non-passive steady states that retain finite ergotropy through population asymmetry. In contrast, DP conserves energy but suppresses coherence entirely, leading to rapid ergotropy loss even when finite internal energy is maintained. This highlights the central role of coherence, rather than energy alone, in governing useful work extraction from quantum batteries.

A comparison of Markovian and non-Markovian dynamics highlights the critical role of reservoir structure in determining long-time battery performance. In the Markovian regime, both energy and ergotropy exhibit rapid initial decay followed by relaxation to modest steady-state values, a signature of irreversible dissipation into a memoryless bath. Introducing non-Markovianity through a time-dependent decay rate substantially alters this behavior. Non-Markovianity enhances long-time ergotropy, when the decay rate retains memory long enough to permit information backflow but still decays sufficiently fast to suppress prolonged dissipation. Very small β leads to strong dissipation, and very large β effectively increases the ergotropy of the system.

Taken together, these findings establish that dissipation is not merely a destructive factor but can be engineered as a resource. Amplitude damping can induce

ergotropy stabilization, and non-Markovian memory effects can prolong useful work extraction. Such insights provide a concrete pathway toward reservoir-engineered graphene quantum batteries, where the combination of coherent charging protocols and structured environments can yield robust nanoscale energy storage devices with enhanced operational efficiency.

APPENDIX A: DENSITY-MATRIX DIAGNOSTICS

To validate the main text results in Sec. IV A, we present tabulated values of the ℓ_1 -coherence C_{ℓ_1} , ergotropy $\mathcal{E}(t)$, and eigenvalue distributions of $\rho(t)$ for selected times t and dissipation strengths γ . These data are obtained directly from numerical simulations and illustrate how population redistribution and coherence loss govern ergotropy retention.

TABLE I: Weak dissipation ($\gamma = 0.1$): time evolution of coherence, ergotropy, and eigenvalue spectrum of $\rho(t)$.

t	C_{ℓ_1}	$\mathcal{E}(t)$	Eigenvalues of $\rho(t)$
0	2.1013	1.8133	{0.353, 0.001, 0.355, 0.291}
10	1.3676	0.9180	{0.33, 0.23, 0.182, 0.258}
40	0.5145	0.1447	{0.265, 0.231, 0.282, 0.222}
100	0.4705	0.1777	{0.270, 0.228, 0.271, 0.231}

TABLE II: Intermediate dissipation ($\gamma = 0.5$): time evolution of coherence, ergotropy, and eigenvalue spectrum of $\rho(t)$.

t	C_{ℓ_1}	$\mathcal{E}(t)$	Eigenvalues of $\rho(t)$
0	2.1013	1.8133	{0.353, 0.001, 0.355, 0.291}
10	1.0078	0.9823	{0.407, 0.099, 0.384, 0.11}
40	0.9983	1.0347	{0.401, 0.103, 0.393, 0.103}
100	0.9983	1.0347	{0.401, 0.103, 0.393, 0.103}

TABLE III: Strong dissipation ($\gamma = 1.0$): time evolution of coherence, ergotropy, and eigenvalue spectrum of $\rho(t)$.

t	C_{ℓ_1}	$\mathcal{E}(t)$	Eigenvalues of $\rho(t)$
0	2.1013	1.8133	{0.353, 0.001, 0.355, 0.291}
10	0.8960	1.7131	{0.453, 0.073, 0.416, 0.058}
40	0.8923	1.7284	{0.453, 0.073, 0.416, 0.058}
100	0.8923	1.7284	{0.453, 0.073, 0.416, 0.058}

APPENDIX B: DISSIPATION-CHANNEL DIAGNOSTICS

To complement the statement in Sec.IV B, we tabulate the ℓ_1 -coherence C_{ℓ_1} , ergotropy $\mathcal{E}(t)$, and eigenvalue distributions of $\rho(t)$ for representative times under amplitude damping (AD) and dephasing (Deph) channels. These results demonstrate how the two noise models differ in their impact on coherence retention, population redistribution, and long-time ergotropy.

TABLE IV: Dephasing (Deph) with weak dissipation ($\gamma = 0.1$).

t	C_{ℓ_1}	$\mathcal{E}(t)$	Eigenvalues of $\rho(t)$
0	2.1013	1.8133	{0.353, 0.001, 0.355, 0.291}
10	0.3469	0.5564	{0.283, 0.308, 0.186, 0.223}
40	0.0160	0.0315	{0.252, 0.251, 0.249, 0.248}
100	0.0000	0.0001	{0.250, 0.250, 0.250, 0.250}

TABLE V: Dephasing (Deph) with strong dissipation ($\gamma = 1.0$).

t	C_{ℓ_1}	$\mathcal{E}(t)$	Eigenvalues of $\rho(t)$
0	2.1013	1.8133	{0.353, 0.001, 0.355, 0.291}
10	0.0888	0.4248	{0.288, 0.222, 0.278, 0.212}
40	0.0111	0.0529	{0.255, 0.246, 0.254, 0.245}
100	0.0002	0.0008	{0.25, 0.25, 0.25, 0.25}

APPENDIX C: MARKOVIAN AND NON - MARKOVIAN CHANNEL DIAGNOSTICS

To complement the analysis in Sec. IV C, we present representative values of the ℓ_1 -coherence C_{ℓ_1} , ergotropy $\mathcal{E}(t)$, and eigenvalue spectra of $\rho(t)$ for Markovian and Non-Markovian reservoirs with $\beta = 0.1, 0.5, 1.0, 5.0$.

These results highlight how memory strength influences coherence retention and population reshaping, thereby determining the long-time work-storage performance.

TABLE VI: (a) Markovian

t	C_{ℓ_1}	$\mathcal{E}(t)$	Eigenvalues
0	2.1012	1.8133	{0.353, 0.001, 0.355, 0.291}
10	1.0066	0.9824	{0.407, 0.099, 0.384, 0.109}
40	0.9983	1.0347	{0.401, 0.103, 0.393, 0.103}
100	0.9983	1.0347	{0.401, 0.103, 0.393, 0.103}

TABLE VII: (b) Non-Markovian ($\beta = 0.1$)

t	C_{ℓ_1}	$\mathcal{E}(t)$	Eigenvalues
0	2.5854	1.7132	{0.226, 0.115, 0.376, 0.282}
10	1.3513	0.7423	{0.242, 0.240, 0.232, 0.286}
40	0.6760	0.4560	{0.211, 0.236, 0.324, 0.228}
100	0.8107	0.4496	{0.245, 0.255, 0.239, 0.262}

TABLE VIII: (c) Non-Markovian ($\beta = 0.5$)

t	C_{ℓ_1}	$\mathcal{E}(t)$	Eigenvalues
0	2.5854	1.7132	{0.226, 0.115, 0.376, 0.282}
10	2.1277	1.1371	{0.213, 0.284, 0.186, 0.317}
40	1.7619	1.1369	{0.075, 0.232, 0.429, 0.265}
100	2.1614	1.1368	{0.264, 0.226, 0.266, 0.244}

TABLE IX: (d) Non-Markovian ($\beta = 1.0$)

t	C_{ℓ_1}	$\mathcal{E}(t)$	Eigenvalues
0	2.5854	1.7132	{0.226, 0.115, 0.376, 0.282}
10	2.3058	1.2817	{0.219, 0.278, 0.191, 0.311}
40	1.8715	1.2817	{0.050, 0.230, 0.447, 0.272}
100	2.3346	1.2816	{0.264, 0.219, 0.276, 0.241}

-
- [1] Kostya S Novoselov, Andre K Geim, Sergei V Morozov, De-eng Jiang, Yanshui Zhang, Sergey V Dubonos, Irina V Grigorieva, and Alexandr A Firsov. Electric field effect in atomically thin carbon films. *science*, 306(5696):666–669, 2004.
 - [2] Gordon W Semenoff. Condensed-matter simulation of a three-dimensional anomaly. *Physical Review Letters*, 53(26):2449, 1984.
 - [3] DP DiVincenzo and EJ Mele. Self-consistent effective-mass theory for intralayer screening in graphite intercalation compounds. *Physical Review B*, 29(4):1685, 1984.
 - [4] Eduardo Fradkin. Critical behavior of disordered degenerate semiconductors. ii. spectrum and transport properties in mean-field theory. *Physical review B*, 33(5):3263, 1986.
 - [5] F Duncan M Haldane. Model for a quantum hall effect without landau levels: Condensed-matter realization of the” parity anomaly”. *Physical review letters*, 61(18):2015, 1988.
 - [6] Kostya S Novoselov, Andre K Geim, Sergei Vladimirovich Morozov, Dingde Jiang, Michail I Katsnelson, Irina V Grigorieva, Sergey V Dubonos, and Alexandr A Firsov. Two-dimensional gas of massless dirac fermions in graphene. *nature*, 438(7065):197–200, 2005.
 - [7] Disha Verma, VS Indrajith, and R Sankaranarayanan. Dynamics of heisenberg xyz two-spin quantum battery. *Physica A: Statistical Mechanics and its Applications*, 1986.

- 659:130352, 2025.
- [8] Thao P Le, Jesper Levinsen, Kavan Modi, Meera M Parish, and Felix A Pollock. Spin-chain model of a many-body quantum battery. *Physical Review A*, 97(2):022106, 2018.
 - [9] Fu-Quan Dou, Hang Zhou, and Jian-An Sun. Cavity heisenberg-spin-chain quantum battery. *Physical Review A*, 106(3):032212, 2022.
 - [10] Giulia Gemme, Gian Marcello Andolina, Francesco Maria Dimitri Pellegrino, Maura Sassetti, and Dario Ferraro. Off-resonant dicke quantum battery: Charging by virtual photons. *Batteries*, 9(4):197, 2023.
 - [11] Alberto Giuseppe Catalano, Salvatore Marco Giampaolo, Oliver Morsch, Vittorio Giovannetti, and Fabio Franchini. Frustrating quantum batteries. *PRX Quantum*, 5(3):030319, 2024.
 - [12] James Q Quach, Kirsty E McGhee, Lucia Ganzer, Dominic M Rouse, Brendon W Lovett, Erik M Gauger, Jonathan Keeling, Giulio Cerullo, David G Lidzey, and Tersilla Virgili. Superabsorption in an organic microcavity: Toward a quantum battery. *Science advances*, 8(2):eabk3160, 2022.
 - [13] I Maillette de Buy Wenniger, SE Thomas, M Maffei, SC Wein, M Pont, N Belabas, S Prasad, A Harouri, A Lemaître, I Sagnes, et al. Experimental analysis of energy transfers between a quantum emitter and light fields. *Physical Review Letters*, 131(26):260401, 2023.
 - [14] Jitendra Joshi and TS Mahesh. Experimental investigation of a quantum battery using star-topology nmr spin systems. *Physical Review A*, 106(4):042601, 2022.
 - [15] James Q Quach and William J Munro. Using dark states to charge and stabilize open quantum batteries. *Physical Review Applied*, 14(2):024092, 2020.
 - [16] Junjie Liu, Dvira Segal, and Gabriel Hanna. Loss-free excitonic quantum battery. *The Journal of Physical Chemistry C*, 123(30):18303–18314, 2019.
 - [17] Francesco Campaioli, Stefano Gherardini, James Q Quach, Marco Polini, and Gian Marcello Andolina. Colloquium: quantum batteries. *Reviews of Modern Physics*, 96(3):031001, 2024.
 - [18] Marius Eich, František Herman, Riccardo Pisoni, Hiske Overweg, Annika Kurzmann, Yongjin Lee, Peter Rickhaus, Kenji Watanabe, Takashi Taniguchi, Manfred Sigrist, et al. Spin and valley states in gate-defined bilayer graphene quantum dots. *Physical Review X*, 8(3):031023, 2018.
 - [19] CH Yang, A Rossi, R Ruskov, NS Lai, FA Mohiyaddin, S Lee, C Tahan, Gerhard Klimeck, A Morello, and AS Dzurak. Spin-valley lifetimes in a silicon quantum dot with tunable valley splitting. *Nature communications*, 4(1):2069, 2013.
 - [20] CWJ Beenakker. Specular andreev reflection in graphene. *Physical review letters*, 97(6):067007, 2006.
 - [21] Kin Fai Mak, Kathryn L McGill, Jiwoong Park, and Paul L McEuen. The valley hall effect in mos2 transistors. *Science*, 344(6191):1489–1492, 2014.
 - [22] Felix Binder, Luis A Correa, Christian Gogolin, Janet Anders, and Gerardo Adesso. Thermodynamics in the quantum regime. *Fundamental Theories of Physics*, 195(1), 2018.
 - [23] Kavalambamalil George Paulson, Hanna Terletska, and Herbert F Fotso. Work extraction from a controlled quantum emitter. *Journal of Physics: Photonics*, 7(2):025023, 2025.
 - [24] Felipe Barra. Dissipative charging of a quantum battery. *Physical review letters*, 122(21):210601, 2019.
 - [25] Zhan-Ning Hu, Kee-Su Park, and Kyung-Soo Yi. Quantum entanglement in a graphene sheet. *J. Korean Phys. Soci*, 54:921, 2009.
 - [26] Dario Ferraro, Michele Campisi, Gian Marcello Andolina, Vittorio Pellegrini, and Marco Polini. High-power collective charging of a solid-state quantum battery. *Physical review letters*, 120(11):117702, 2018.
 - [27] Francesco Campaioli, Felix A Pollock, Felix C Binder, Lucas Céleri, John Goold, Sai Vinjanampathy, and Kavan Modi. Enhancing the charging power of quantum batteries. *Physical review letters*, 118(15):150601, 2017.
 - [28] VS Indrajith, R Muthuganesan, and R Sankaranarayanan. Fidelity-based purity and coherence for quantum states. *International Journal of Quantum Information*, 20(06):2250016, 2022.
 - [29] Armen E Allahverdyan, Roger Balian, and Th M Nieuwenhuizen. Maximal work extraction from finite quantum systems. *Europhysics Letters*, 67(4):565, 2004.
 - [30] Gianluca Francica, John Goold, Francesco Plastina, and Mauro Paternostro. Daemonic ergotropy: Enhanced work extraction from quantum correlations. *npj Quantum Information*, 3(1):12, 2017.
 - [31] Heinz-Peter Breuer and Francesco Petruccione. *The theory of open quantum systems*. OUP Oxford, 2002.
 - [32] Daniel Manzano. A short introduction to the lindblad master equation. *Aip advances*, 10(2), 2020.
 - [33] Michael A Nielsen and Isaac L Chuang. *Quantum computation and quantum information*. Cambridge university press, 2010.
 - [34] Tillmann Baumgratz, Marcus Cramer, and Martin B Plenio. Quantifying coherence. *Physical review letters*, 113(14):140401, 2014.
 - [35] Barış Çakmak. Ergotropy from coherences in an open quantum system. *Physical Review E*, 102(4):042111, 2020.
 - [36] Srijon Ghosh, Titas Chanda, Shiladitya Mal, and Aditi Sen. Fast charging of a quantum battery assisted by noise. *Physical Review A*, 104(3):032207, 2021.
 - [37] Crispin Gardiner and Peter Zoller. *Quantum noise: a handbook of Markovian and non-Markovian quantum stochastic methods with applications to quantum optics*. Springer Science & Business Media, 2004.
 - [38] Maximilian Schlosshauer. *Decoherence and the quantum-to-classical transition*. Springer, 2007.
 - [39] JMZ Choquehuanca, PAC Obando, FM de Paula, and MS Sarandy. Qubit dynamics of ergotropy and environment-induced work. *Physical Review A*, 109(5):052219, 2024.
 - [40] Nicolai Friis and Marcus Huber. Precision and work fluctuations in gaussian battery charging. *Quantum*, 2:61, 2018.